Authors' accepted manuscript
Article published in *Journal of Thermophysics and Heat Transfer* (28 sept. 2021)
The final published version is available at: https://doi.org/10.2514/1.T6389

Frossling Number Assessment for an Airfoil Under Fully Turbulent Flow Conditions

Abdallah Samad*
Univeristy of Quebec in Chicoutimi, 555 University Boulevard, Chicoutimi, Quebec, G7H 2B1, Canada

Gitsuzo B. S. Tagawa†, Rasoul Rajabi Khamesi‡ and François Morency§
Univeristy of Quebec, School of Superior Technology, 1100 Notre-Dame St W, Montreal, Quebec, H3C 1K3, Canada

and
Christophe Volat**
Univeristy of Quebec in Chicoutimi, 555 University Boulevard, Chicoutimi, Quebec, G7H 2B1, Canada

North American winters are notorious for aircraft icing, which is a direct threat to aviation safety. Existing high-fidelity codes successfully model icing/de-icing simulations and calculate convective heat transfer, with a penalty of a high computational cost. For a conceptual design of an ice protection system however, correlations offer a quick approach to determine the average heat transfer rate on an airfoil. The objective of this paper is to introduce a novel correlation for the Frossling Number on a NACA 0012, under fully turbulent flow conditions. The correlation is the result of curve fitting a heat transfer database, created using CFD simulations and valid for a wide range of Reynolds Numbers and angles of attack. Moreover, the effects of using two different turbulence models as well as two different thermal boundary conditions are investigated. A flat plate test case is used to verify the heat transfer prediction, and airfoil simulations are validated with experimental measurements at the stagnation point. The final form of the correlation shows that a cubic variation of α fits the CFD data best, with an average error of 2.14%.

* Postdoctoral Researcher, Anti-icing Materials International Laboratory (AMIL), Department of Applied Sciences.
† PhD, Thermo-Fluids for Transport Laboratory (TFT), Mechanical Engineering Department.
‡ PhD Student, Thermo-Fluids for Transport Laboratory (TFT), Mechanical Engineering Department.
§ Professor, Thermo-Fluids for Transport Laboratory (TFT), Mechanical Engineering Department.
** Professor, Anti-icing Materials International Laboratory (AMIL), Department of Applied Sciences.

Nomenclature

A, *B*, *C*, *D*, and *m* = Correlation Coefficients

SA = Spalart-Allmaras

SST = Menter's Shear Stress Transport

Nu = Nusselt Number

Fr = Frossling Number

Re = Reynolds Number

Pr = Prandtl Number

α = Angle of Attack (°)

V = Velocity (m/s)

h = Heat Transfer Coefficient ($W/m^2.K$)

Q = Heat Flux (W/m^2)

T = Temperature (K)

S/c = Non-dimensional wrap distance

c = Chord (m)

TBC = Thermal Boundary Condition

c_p = Specific Heat Capacity

C_f = Friction Coefficient

C_L = Lift Coefficient

C_D = Drag Coefficient

Subscripts

$_{TM}$ = turbulence model

$_{S}$ = Surface

$_{rec}$ = Recovery

$_{f}$ = Film

$_{\infty}$ = Freestream Value

$_{x}$ = Local Value

$_{Avg}$ = Average Value

I. Introduction

The importance of ice protection systems grows proportionally with the ever-increasing need for air travel and transport. The advent of computers in the early 1980's made the resolution of the Navier-Stokes equations possible, leading to the emergence of icing/de-icing codes. With the turn of the new millennium, several icing/de-icing tools have been developed internationally such as LEWICE [1], ONERA [2, 3], FENSAP-ICE [4] and CANICE [5, 6]. Between each other, these codes can conduct icing/de-icing simulations for problems ranging from isolated wings to rotors and complete aircraft configurations [7-12].

CFD based icing codes utilize significant computer power and are time consuming. They usually calculate the convective heat transfer through the direct solution of the Reynolds-Averaged Navier–Stokes (RANS) equations. While the accuracy of these codes is unparalleled and crucial for ice protection systems development, correlations still offer an interesting approach, especially in the early stages of design. Moreover, if only the average rate of heat transfer on the airfoil is needed, the correlation could help navigate modeling uncertainties. In this work, a correlation is developed to be later used to estimate the power requirement for ice protection systems.

The literature provides well-established correlations for the convective heat transfer on flat plates, cylinders and spheres [13, 14]. They represent the non-dimensional heat transfer by the Nusselt (Nu) or (Fr) Frossling Numbers, where $Fr = Nu \times Re^{-0.5}$. The general form of those correlations (in their local or average values) is based on equation (1), where the product of the Reynolds (Re) and Prandtl (Pr) numbers is associated with parameters (A) and (m) that are often determined empirically. The m values are usually associated with the flow condition, depending on whether it's laminar ($m = 0$), turbulent ($m > 0$) or transitional ($m < 0$) [15]. The Thermal Boundary Condition (TBC) affects the A values and in the case of the flat plate, the constant surface heat flux (Q_S) leads to A values about 4% higher than the constant surface temperature (T_S) [13, 14].

$$Fr = A \times \mathrm{Re}^{m} \times \mathrm{Pr}^{1/3} \tag{1}$$

Fixed wing airfoils have more parameters to model than a flat plate mainly due to the added thickness as well as the effects of angles of attack (α). Nevertheless, the literature indicates airfoil heat transfer has been extensively

studied. In the work of *Poinsatte et al.* [16], the leading edge (L.E.) of a smooth NACA 0012 was fitted with embedded heating gauges located between -3.6% and 9.5% of the dimensionless wrap distance (*S/c*), keeping it at constant T_S *TBC*. A total of 46 tests was done between the Icing Research Tunnel (IRT) as well as in-flight measurements of the NASA Lewis Twin Otter icing research aircraft by *Newton et al.* [17]. For a range of $-6° \leq \alpha \leq 8°$ and $1.2\times10^6 \leq Re \leq 2.4\times10^6$, they measured the heat transfer and showed that the local Fr_x curves collapse into one near the L.E., making the Fr_x independent of Re_x. This was confirmed by the successful correlation of Fr_x at each *S/c* with *Re* based on equation (1), where the *m* was found to be $m = 0$. *Henry et al.* [18] utilized equation (1) to partially correlate the measured heat transfer coefficients for different ice shapes on an iced airfoil for a range of $1.25\times10^6 \leq Re \leq 1.9\times10^6$. *Dukhan* [19] experimented on two NACA0012 airfoil shapes for $\alpha = 0°$, each with a different roughness representation of glaze ice with horns for $4\times10^5 \leq Re \leq 1.54\times10^6$. The measured Fr_x was correlated at three different location: the stagnation point, around the horn and after the horn. *Wang et al.* experimented on a hollowed NACA 63-421 equipped with heating strips installed on the inner edges of the airfoil that transferred a constant Q_S by conduction through the airfoil skin to the airflow. Using 25 thermocouples distributed across the chord on the exterior and interior surfaces, they calculated the average Nusselt number (Nu_{Avg}) at $\alpha = 0°$ [20] as well as $0° \leq \alpha \leq 25°$ [21]. In both works, they used equation (1) to correlate their data. Their main contribution was in the expansion of the *A* term in the equation to account for the α. *Li et al.* [22] measured the static pressure and heat transfer rates on a BO 28 airfoil with 23 embedded heating tiles, covering up to 90% of the surface. The measurements were at a constant T_S *TBC* with a range of $8.5° \leq \alpha \leq 19.5°$ and $Re = 2.5\times10^5$, 5.82×10^5 and 1.085×10^6. Their wide range of measurements captured the variation of the Fr_x in the laminar, transitional and turbulent regions of the flow. High Fr_x values were seen on the stagnation point that decreased in the laminar region downstream. The Fr_x was independent of *Re*, confirming the findings of [16]. The transient region was characterized with a rapid increase of Fr_x, showing the highest values across the chord. The abrupt increase of Fr_x at the transition point was followed by a less severe yet rapid decrease of Fr_x values downstream towards the T.E..

Although heat transfer on airfoils was well studied, to the best of the author's knowledge, the literature lacks correlations for the average heat transfer for airfoils with a fully turbulent flow. Therefore, the main objective of this paper is to propose a correlation for the Fr_{Avg} on an airfoil, based on CFD simulations under fully turbulent flow conditions. *Stanford University Unstructured SU2* [23] is used to run three sets of CFD simulations on a 2-D airfoil. The first and second set of simulations are both for a constant Q_S *TBC*, but each uses a different turbulence model

(fully turbulent SST_{TM} and fully turbulent SA_{TM}). The final set uses a wide range of *Re* and α with a constant T_S *TBC* and the SA_{TM}. The novel correlation of this work is based on the final set of simulations.

In the following sections, the CFD model used and the methodology followed to calculate the convective heat transfer are presented. The proposed form of correlation is then detailed. In the results section, the flat plate verification test case is examined first. Followed by a validation with experimental data of a NACA 0012 airfoil. The effects of *Re*, α and *TBC* on the local and average *Fr* are then investigated. Finally, the curve fitting results are used to present the final form of Fr_{Avg} correlation for airfoils. In this paper, all curves fitting are done using MATLAB curve fitting toolbox [24].

II. Methodology

A. Mathematical & Numerical Scheme

SU2 is an open-source collection of codes developed in C++ designed to numerically solve problems described by Partial Differential Equations (PDEs) [23]. In this work, the compressible RANS flow equations are solved to compute the heat transfer and the temperature at the wall of the simulated airfoil. The fluid model is set to standard air. The static pressure *P* is related to the temperature *T* and the density ρ via the ideal gas law with the specific gas constant R = 287.058 *N.m/kg.K*. The caloric equation of state for ideal gas relates the energy to the pressure and density $\rho = c_v T = P/\rho(\gamma - 1)$, with γ = 1.4 and $c_v = R/(\gamma - 1)$. The dynamic viscosity μ_d follows the *Sutherland Law*.

The development of RANS equations yields six extra unknowns. In this paper, the two turbulence models used rely on the *Boussinesq Hypothesis* [25] to close the system of equations. The total viscosity replaces the dynamic viscosity to compute the viscous stresses, such that $\mu_T = \mu_d + \mu_t$. The turbulent viscosity μ_T is obtained from either the one-equation *Spalart-Allmaras* (SA_{TM}) [26], or the two-equation *Menter's Shear Stress Transport* (SST_{TM}) [27]. Both are used without any transition model, mainly to model a fully turbulent flow on the airfoil and all the way from the leading edge.

The space numerical integration uses a *HLLC* scheme for the inviscid terms of the RANS equations with a second order MUSCL scheme and a Venkatakrishnan slope limiting method. A second order Least-Squares reconstruction method is used for the viscous terms. For the turbulence equation, a scalar upwind scheme is used for

the inviscid terms and a second order integration for the viscous terms. For the local time stepping, the time numerical integration uses an Euler implicit method with a constant *Courant-Friedrichs-Lewy* number *CFL* = 2.5. Calculations are run for 400,000 iterations with a residual below 10^{-7}.

B. Geometry Discretization

The discretized airfoil undergoing forced convection is shown in Figure 1. When a freestream of air passes with a velocity V_∞ and temperature T_∞ over it, an exchange of heat will exist between the airfoil surface and the air. For the considered cases of CFD simulations previously described, the airfoil wall is discretized into *N* points, as seen in the figure, with the locations of each point in the domain in the *x* and *y* directions known.

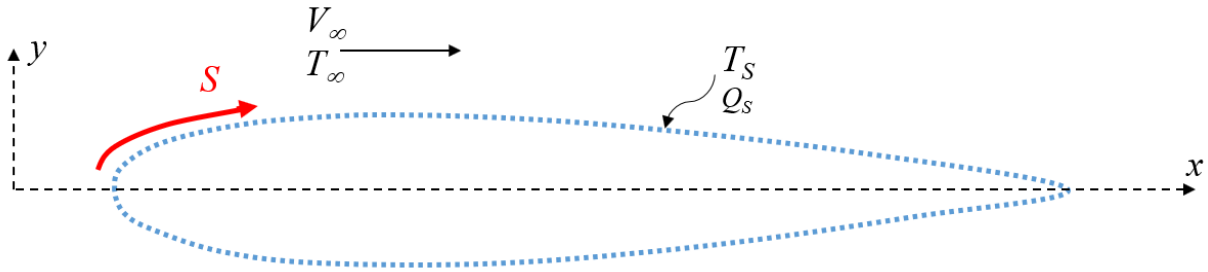

Figure 1 Representation of Discretized Points on Airfoil Wall with Convection

For results presentation, the location on the airfoil wall is defined by the non-dimensional curvilinear distance *S/c*. It represents the true length on the airfoil wall. If the airfoil is discretized into *N* points, then *S* is calculated using equation (2). The curvilinear value at point $x = 0$ is then subtracted to center the curvilinear coordinate around the airfoil leading edge. A positive sign is adopted for the *S* on the upper surface and a negative indicated that the *S* is considered on the bottom surface.

$$S_i = \begin{cases} 0 & i = 1 \\ \sum_{2}^{N} \sqrt{(x_i - x_{i-1})^2 + (y_i - y_{i-1})^2} & i > 1 \end{cases} \tag{2}$$

C. Convective Heat Transfer Calculation

To estimate the convection rate, Newton's Law of Cooling is applied to the results of the 2D CFD simulations. At each discretized point *i* (with a specific $T_{S,i}$ or $Q_{S,i}$), equation (3) is applied to calculate the local heat transfer coefficient $h_{x,i}$. The recovery temperature T_{rec} is used in that equation to account for the effect of air velocity on heat transfer. In this work, the flow is considered fully turbulent, so the recovery coefficient is set at $r_{coeff} = Pr^{1/3}$,

according to [14]. The relation between T_{rec} and T_∞ is described in equation (4) where the specific heat capacity of air is c_P = 1006 *kJ/kg.K*. The thermal properties of air (density ρ, viscosity μ and thermal conductivity k) are evaluated at a film temperature T_f using equation (5). The average heat transfer coefficient h_{Avg} is then obtained by equation (6), where ΔS_i is the curvilinear distance between points i and i +1.

$$h_{x,i} = \frac{Q_{S,i}}{\left(T_{S,i} - T_{rec}\right)} \tag{3}$$

$$T_{rec} = T_\infty \left(1 + r_{coeff} \frac{V_\infty^2}{2c_P}\right) \tag{4}$$

$$T_f = \frac{T_{rec} + T_{S,i}}{2} \tag{5}$$

$$h_{Avg} = \frac{1}{c} \sum_{i=1}^{N} h_{x,i} \times \Delta S_i \tag{6}$$

With the calculated heat transfer coefficient, the Nusselt Number could then be calculated by its local (Nu_x) or average (Nu_{Avg}) values using equation (7). Finally, the local (Fr_x) and average (Fr_{Avg}) Frossling Numbers are calculated using equation (8). The Re_c used is based on the chord as defined by equation (9).

$$Nu_x = \frac{h_x c}{k} \quad Nu_{Avg} = \frac{h_{Avg} c}{k} \tag{7}$$

$$Fr_x = \frac{Nu_x}{\sqrt{\mathrm{Re}_c}} \quad Fr_{Avg} = \frac{Nu_{Avg}}{\sqrt{\mathrm{Re}_c}} \tag{8}$$

$$\mathrm{Re}_c = \frac{\rho V_\infty c}{\mu} \tag{9}$$

D. Grid Selection

The grids used in this study are from *NASA* [28]. Three grids (type C-Grid) were evaluated, identified here as coarse (225 × 65 nodes), medium (449 × 129 nodes) and fine (897 × 257 nodes). The space at the wall, for the finest grid, was y/c =2 x 10^{-6}, which resulted in $y^+ \approx 0.1 \sim 0.2$. The finest grid counts 257 points on the airfoil surface while the coarsest grid counts 65.

A mesh study was performed to assess the impact of the grid size on the calculated Fr_{Avg}, C_L and C_D. The mesh types and corresponding evaluated values of the assessed parameters are described in Table 1. The test case consisted of the NACA 0012 with $Re = 1\times10^6$ and $\alpha = 0°$.

Table 1 Values of the Fr_{Avg}, C_L and C_D Obtained by the Three Assessed Grids, along with the Corresponding Fine Grid Convergence Index GCI^{21}_{fine}

Type of Grid	Mesh Size	Fr_{Avg}	C_L	C_D
Coarse	225 × 65	1.8445	-0.000002	0.01036
Medium	449 × 129	1.8486	-0.000002	0.01043
Fine	897 × 257	1.8594	-0.000002	0.01095
GCI^{21}_{fine}		0.45%	0.00%	0.89%

The method of [29] was followed to calculate the fine grid convergence index GCI^{21}_{fine}, which is also presented in Table 1. Based on the grid study and the assessment of the three different meshes, Table 1 indicates that the reported values for Fr_{Avg}, C_L and C_D in this work, have respective uncertainties of 0.45%, 0% and 0.89%.

E. Proposed Form of the Airfoil Frossling Number Correlation

As the introduction pointed out, flat plates and cylinders have been successfully correlated by equation (1) in the past. For airfoils, experimental work by [21] expanded that form of equation to include a term for the variation of α. They proposed a correlation for the Fr_{Avg} on a NACA 63-421 airfoil with a linear variation of α as shown in equation (10).

$$Fr_{NACA63-421} = \begin{cases} 0.094\times(0.75+0.017\times\alpha)\,\mathrm{Re}^{0.136}\times\mathrm{Pr}^{1/3} & \mathrm{Re} > 5\times10^5 \\ 2.482\times(0.75+0.013\times\alpha)\,\mathrm{Re}^{-0.189}\times\mathrm{Pr}^{1/3} & \mathrm{Re} \le 5\times10^5 \end{cases} \quad (10)$$

The main interest of this work is the heat transfer correlation for a NACA 0012 airfoil. Using the flat plate or cylinder correlation as an approximation to calculate heat transfer on airfoil would not represent the geometry correctly and can not consider α effects. Moreover, and while the linear variation of α in equation (10) suits the NACA 63-421 well, the results of this work indicate otherwise for the NACA 0012. Therefore, a new correlation for the NACA 0012, that correctly captures the CFD predicted variation of Fr_{Avg} with α is sought. The new correlation implies that the Fr_{Avg} would be better represented with a cubic variation of α, in the form of equation (11), as will be seen in section IV. *A*, *B*, *C*, *D* and *m* are the correlation parameters determined based on a curve fitting method.

$$Fr_{Avg} = A\left(1 + B \times \alpha_{Eff} + C \times \alpha_{Eff}^{2} + D \times \alpha_{Eff}^{3}\right) \mathrm{Re}^{m}\, \mathrm{Pr}^{1/3} \tag{11}$$

In that scope, the present work uses the results of CFD simulations on a NACA 0012 to build a correlation for the Fr_{Avg}. Each CFD simulation produces a specific Fr_{Avg} for each unique combination of the *Re* and α. These data are in turn used to build a correlation in the proposed form of equation (11).

III. Results

The presented results are categorized into three parts. First, a flat plate test case is simulated, and verification is done on the calculated C_f and *Fr*. Second, the NACA 0012 simulations are done with SA_{TM}, and verification and validation are done on the calculated viscous data (C_L and C_D) as well as *Fr* at the stagnation point. Finally, the airfoil heat transfer effects are analyzed based on: 1– the thermal boundary condition and the use of a different turbulence model; 2- the angle of attack α and 3- the Reynolds number *Re*.

A. Flat Plate Verification Test Case

The verification flat plate test case uses the grid by *NASA* [30]. The length of the plate is 2 meters and the full-length Re_L is 1×10^7. The Mach number used is $Ma = 0.15$. Two *TBC*s are examined; first, the constant T_S *TBC* with $T_S = 280$ K and $T_\infty = 300$ K and second, the constant Q_S *TBC* with $Q_S = 2000$ W/m^2 and $T_\infty = 281.66$ K. In both cases, the flat plate wall is discretized with 450 elements.

1. Friction Coefficient

Two correlations from the literature are used to verify the results of the C_f from the flat plate CFD simulations. The C_f correlations are described by equations (12) and (13), both from [14] and are for a constant T_S *TBC*. Figure 2 shows the C_f variation across the length of the plate (represented by the local Re_x), as calculated either by correlations or by CFD.

$$C_f / 2 = 0.0287\, \mathrm{Re}_x^{-0.2} \tag{12}$$

$$C_f / 2 = 0.185 (\log_{10} \mathrm{Re}_x)^{-2.584} \tag{13}$$

Figure 2 shows an agreement between the results of CFD and the correlations. The discrepancy between the two sets of data varied between a maximum of 6% for $Re_x < 3 \times 10^6$ and 2% for higher Re_x. The CFD results are then verified and predict C_f values similar to those of previous studies.

New correlations for the C_f could be proposed based on the CFD results of this work. This is presented by equation (14) and equation (15), both valid for $0 \leq Re_x \leq 10^7$. The new correlations are obtained by curve fitting the CFD results based on the form of equation (12). The correlations are for flat plates with constant T_S and constant Q_S *TBC*s and fit the CFD data with an error of 0.94% and 0.95%, respectively. By comparing equations (14) and (12), Figure 2 shows how the CFD data decrease slower than those of equation (12), leading to higher discrepancy with Re_x and thus explaining the different power term associated with each correlation.

$$C_f/2 = 0.0232\,\mathrm{Re}_x^{-0.14} \tag{14}$$

$$C_f/2 = 0.0236\,\mathrm{Re}_x^{-0.1404} \tag{15}$$

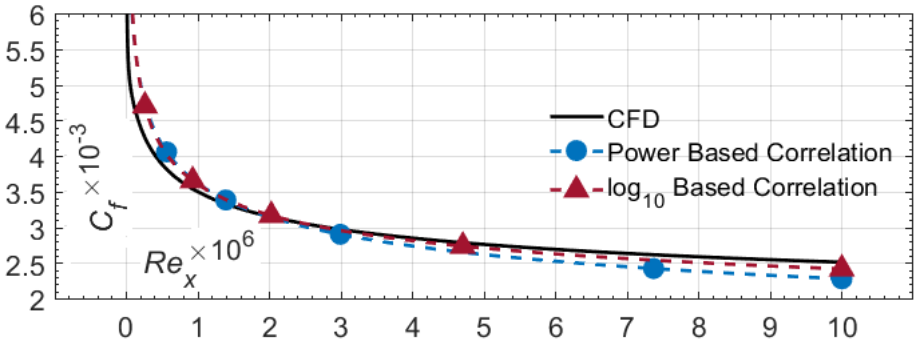

Figure 2 Flat Plate Comparison of C_f versus Re_x for a constant T_S *TBC*

2. Frossling Number

The predicted heat transfer results for the flat plate test case are also verified. For the case of a constant T_S, CFD results are compared to flat plate correlations from the literature with the same *TBC*. The correlations correspond to equations (16) and (17) [13, 14].

$$Fr_x = 0.0296\,\mathrm{Re}_x^{4/5}\,\mathrm{Pr}^{1/3}/\sqrt{\mathrm{Re}_L} \tag{16}$$

$$Fr_x = 0.0287\,\mathrm{Re}_x^{4/5}\,\mathrm{Pr}^{0.6}/\sqrt{\mathrm{Re}_L} \tag{17}$$

Figure 3 shows the Fr_x variation versus the increasing Re_x across the plate length. The Fr_x increases across the plate due to an increase of the Re_x. The discrepancy between the CFD results and the correlation of [13] is around 7% for all Re_x. The discrepancy compared to the correlation of [14] is around 7% for $Re_x < 5\times10^6$ and 12% for $Re_x > 5\times10^6$. Given the 15% accuracy of either correlation, the discrepancy found with CFD results is satisfactory.

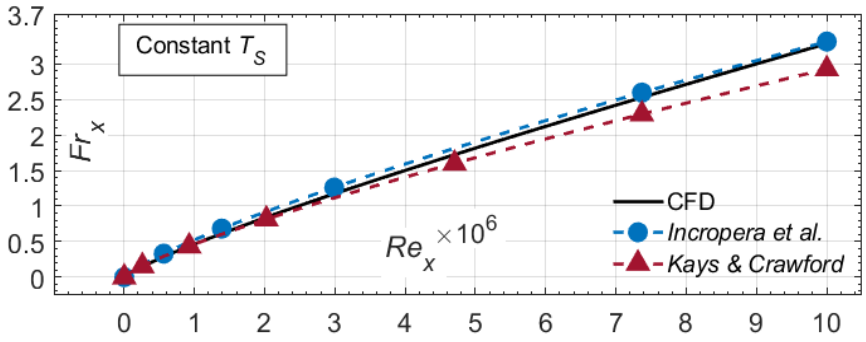

Figure 3 Comparison between CFD and Correlation Results of the Fr_x vs. Re_x for a Flat Plate with Constant T_S TBC

Having verified the CFD results of this work, a new correlation for the Fr_x on the flat plate could be formed, based on a curve fitting of the CFD data and similar to what was proposed earlier for the C_f. Valid for $0.5 \times 10^6 \leq Re_x \leq 10^7$, equations (18) represents the Fr_x on a flat plate with constant T_S and fit the CFD data with an error of 0.49%. By comparing equations (18) and (16), Figure 3 shows how the two correlations show less than 7% for all Re_x and thus the verification shows that CFD correlations are close to the empirical correlations of the literature.

$$Fr_x = 0.0141 \times \mathrm{Re}_x^{4.25/5} \times \mathrm{Pr}^{1/3} \Big/ \sqrt{\mathrm{Re}_L} \tag{18}$$

The flat plate test case is also verified using a constant Q_S *TBC*, heat transfer results from two other implementations of the SA_{TM} from the literature are used. These correspond to the numerical results of [31] and [32]. Both provided the local Stanton Number St_x for a constant Q_S *TBC*. The St_x is transformed into the Fr_x by $Fr_x = \left(St_x \, \mathrm{Re}_x \, \mathrm{Pr}\right) \Big/ \sqrt{\mathrm{Re}_L}$. As seen in Figure 4, the SA_{TM} implementation of this work as well as those from the literature all provide similar results, with no more than 2% discrepancy. The different discretization of each numerical implementation is the reason why the discrepancy exists; however, the comparison shows acceptable prediction of the heat transfer using the CFD simulations of this work.

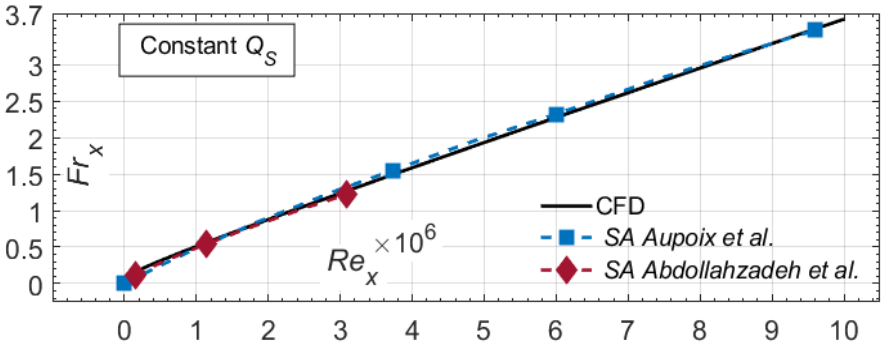

Figure 4 Comparison between CFD and Correlation Results of the Fr_x vs. Re_x for a Flat Plate with Constant Q_S *TBC*

B. Validation & Verification: NACA 0012 CFD Simulations

The main simulations for the NACA 0012 use the computational domain defined by *NASA* [30]. The chord is c = 1 m and the turbulence model used is the SA_{TM}. The far field boundary is located 500 chords away from the airfoil. The airfoil wall is discretized with 512 elements and the far field with 1408 elements. The Mach Number is Ma = 0.15, the freestream temperature is T_∞ = 281.66 K and α is varied between 0° and 30° to account for stall effects. The *TBC* is a constant T_S, Re is varied between 2×10^5 and 3×10^6 and T_s = 273.15 K.

1. *Lift & Drag*

Figure 5 shows the comparison between the C_L and C_D from the CFD simulations versus numerical and experimental results from the literature. Figure 5a is for the C_L variation with α while Figure 5b shows the variation of C_D with C_L. The numerical results of OVERFLOW and CFL3D are obtained from [33] whereas the experimental data were from [34].

The numerical results from SU2 almost match those of OVERFLOW and CFL3D, with the error being less than 1% for either C_L or C_D. When compared to experimental data, *SU2* tends to overpredict the C_L and C_D. The maximum error occurs at α = 10°, at 1.64% for the C_L and 5.59% for the C_D. *SU2* also presents a good estimation of the maximum lift coefficient $C_{L(max)}$, being 1.66 at α = 17° versus 1.64 for the experimental data, resulting in an error of 1.2%. The error produced by *SU2* is then comparable to that of other numerical tools and falls within an

acceptable range of experiments, confirming the capability of *SU2* in simulating viscous flow effects on the NACA 0012.

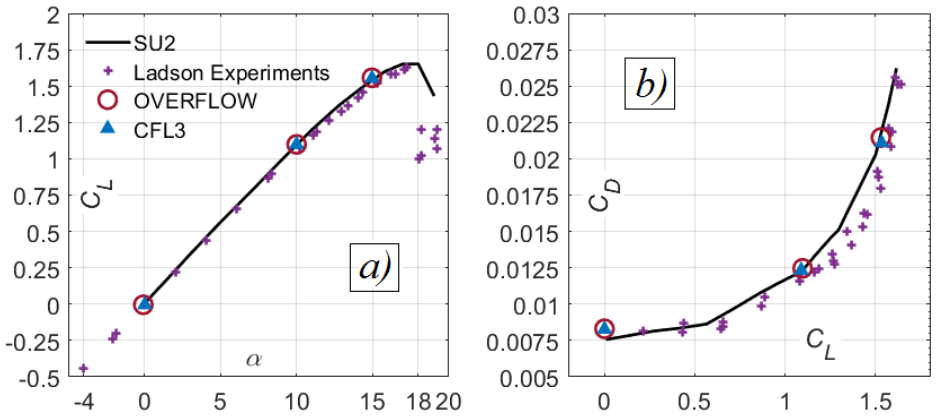

Figure 5 Numerical & Experimental Comparison of NACA 0012 Viscous *a*) C_L versus α and *b*) C_D versus C_L

2. Frossling Number

The CFD heat transfer data are compared to experimental measurements at the stagnation point and near the leading edge ($-0.03 \leq S/c \leq 0.08$) of a NACA 0012 [16]. The Fr_x comparison is shown in Figure 6 where three different *Re* are presented, all at $\alpha = 0°$. Both the CFD data and the experimental values are for a flow under a constant T_S TBC.

The main interest of the comparison lies at the stagnation point. According to [16], the Fr_x at $S/c = 0$ is independent of *Re* nor is affected by the flow condition. Therefore, the fully turbulent simulations should predict Fr_x values at $S/c = 0$ that are similar to the experiments. This is confirmed by examining Figure 6, where the CFD values agree with the experimental data within 8%. Moreover, both sets of data show unchanging Fr_x values with *Re* at $S/c = 0$, consistent with the Fr_x behavior at the stagnation point.

In regard to why the fully turbulent CFD data in Figure 6 deviate from their experimental counterparts downstream of $S/c = \pm 0.02$, previous studies showed that Fr_x is independent of *Re* for a laminar flow, while this is not the case for a turbulent flow [13, 14, 16]. For the experiments, the Fr_x changes only with S/c, while the numerical results show that Fr_x also increases with *Re*. Therefore, the curves of Fr_x are reduced into one for the experiments (laminar; $Fr_x \propto Re^0$), while the fully turbulent CFD simulations show varying Fr_x values with *Re* ($Fr_x \propto Re^{0.43}$).

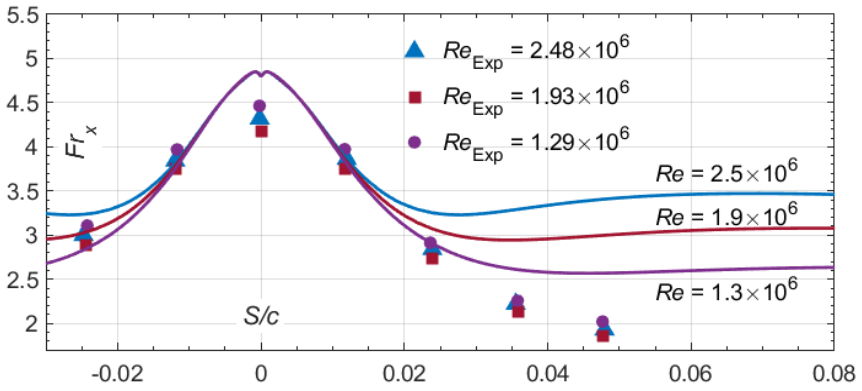

Figure 6 Leading Edge NACA 0012 CFD Data Versus Experimental NACA 0012 Measurements

C. Heat Transfer Effects: NACA 0012 CFD Simulations

1. Turbulence Model & Thermal Boundary Condition

In this section, the effects of changing the *TBC* on the surface on the airfoil from a constant T_S to a constant Q_S is investigated. The constant Q_S simulations had Q_S = 2000 W/m^2 and T_∞ = 281.66 K. Two turbulence models are used: the SA_{TM} and SST_{TM}. For the SA_{TM} simulations, one *Re* ($Re = 1 \times 10^6$) is used together with the same range of α as the simulations with constant T_S ($0° \le \alpha \le 30°$). For the SST_{TM} simulations, one α ($\alpha = 0°$) is used together with a range of $3 \times 10^5 \le Re \le 3 \times 10^6$ and then one *Re* ($Re = 1 \times 10^6$) is used together with a range of $0° \le \alpha \le 30°$. Aside from quantifying the difference between the use of two *TBC*s, this analysis also serves as a verification on the heat transfer results by comparing the Fr_x obtained by two different turbulence models.

Figure 7a shows the results of simulations in terms of the Fr_x variation across the whole airfoil while Figure 7b shows a closeup of the variation near the leading edge. The Fr_x is compared for three cases: 1- SA_{TM} with constant T_S; 2- SA_{TM} with constant Q_S; and 3- SST_{TM} with constant Q_S. All three cases are for $Re = 1 \times 10^6$ and $\alpha = 0°$.

The Fr_x from the three test cases are similar on an examination of the overall variation on the airfoil. Comparing the SA_{TM} model with constant T_S or constant Q_S, the main difference is the Fr_x values that are between 2% and 4% lower between $0 < S/c \le \pm 0.3$. At the stagnation point, the simulation with constant Q_S shows an Fr_x value almost 8% lower than the case of constant T_S. Later, the Fr_x almost matches between the two test cases further downstream and all the way to the trailing edge, although a discrepancy between 2% and 4% is found.

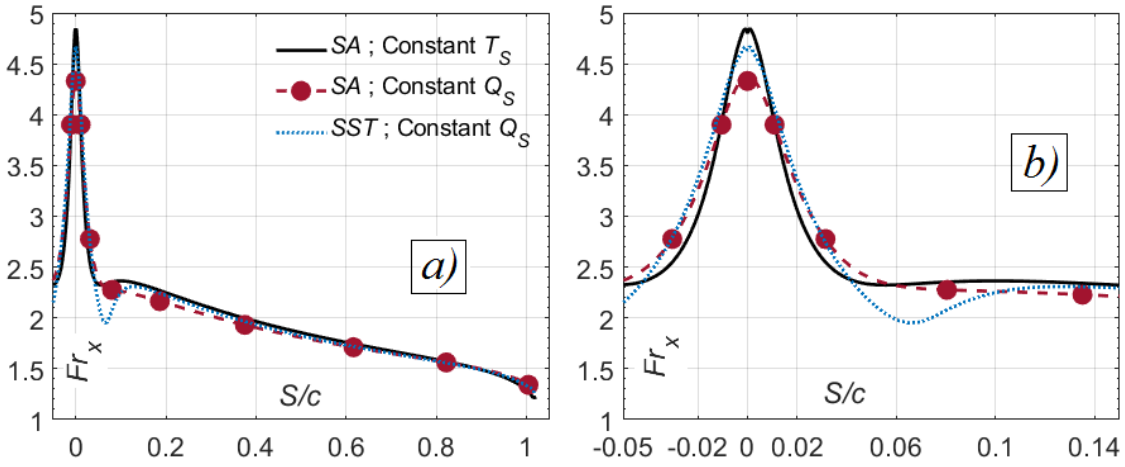

Figure 7 Comparison of Fr_x Variation on NACA 0012 under constant Q_S & T_S *TBC*s

For the SST_{TM} with constant Q_S, a more significant difference is observed. On the leading edge, it is noted that the Fr_x value at the stagnation point (S/c = 0) is also different from the other two test cases. Compared to the SA_{TM} with constant Q_S, the SST_{TM} had a 4% lower prediction of the Fr_x. Furthermore, the Fr_x is almost the same between 0 < S/c ≤ ± 0.03 compared to the SA_{TM} with constant Q_S. However, a "dip" is seen between 0.03 < S/c ≤ ± 0.1 where the SST_{TM} predicts lower values, especially around S/c ≈ 0.06. Here, the Fr_x values are almost 20% lower than the other test cases. This is then followed by an increase of Fr_x, the data from all simulations later match all the way to the trailing edge.

The average Fr_{Avg} is also computed for each of the simulated test cases. Figure 8a shows the results of Fr_{Avg} as a function of the increasing *Re* at $\alpha = 0°$. The results of both turbulence models and both *TBC*s are compared. Similar to the constant Q_S with SA_{TM}, the SST_{TM} implementation predicts Fr_{Avg} that are around 3% lower than the constant T_S *TBC*, especially for the lower *Re*. It is therefore determined that although the SST_{TM} showed a slightly different behavior than the SA_{TM} on a local level, the Fr_{Avg} by the two turbulence models varied between 3% to 5%.

Similarly, Figure 8b shows the results of Fr_{Avg} as a function of the increasing α for the constant T_S and Q_S simulations at $Re = 1 \times 10^6$, for both turbulence models. For the simulations with the SA_{TM}, there is no significant change in the behavior of the Fr_{Avg} for different *TBC*s. However, the constant Q_S simulations always underpredict the constant T_S by around 3%.

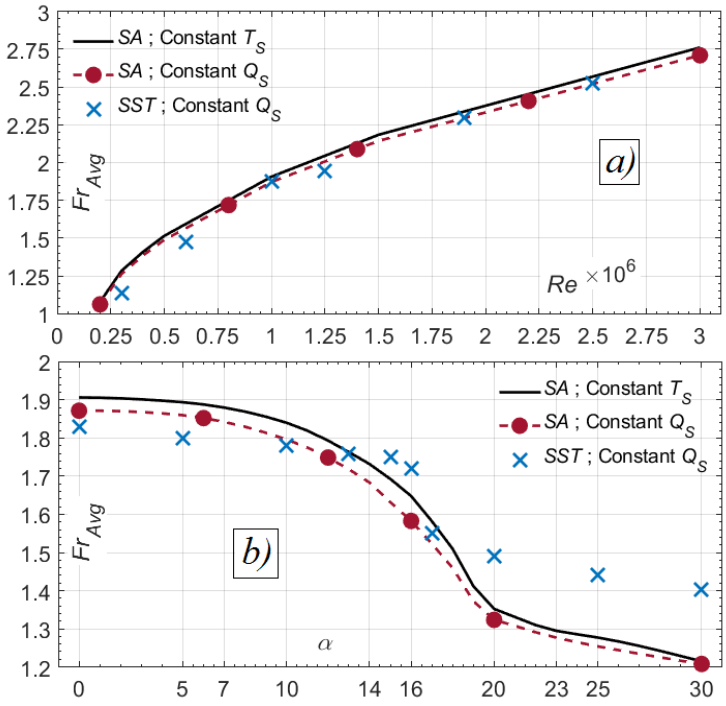

Figure 8 Comparison of NACA 0012 Fr_{Avg} under constant Q_S & T_S TBCs for $Re = 1 \times 10^6$

On the other hand, when the SA_{TM} and SST_{TM} implementations from Figure 8b are compared, a significant change is observed. For $\alpha \leq 10°$, the SST_{TM} predicts Fr_{Avg} values around 5% lower of those of the SA_{TM}. On the other end, the values of the SST_{TM} are up to 17% higher than those of the SA_{TM} for $\alpha \geq 20°$. The turbulence models also show different Fr_{Avg} values around the angle where stall first appears, between $13° \leq \alpha \leq 17°$. In this region, the discrepancy reaches a maximum of around 7%. Also, the decrease of values is sharper for the SST_{TM} compared to the SA_{TM}.

The preceding analysis shows how the different turbulence models impact the predicted values of Fr. Although the overall decreasing behavior with α was consistent between the SA_{TM} and SST_{TM}, the discrepancy varied between 5% and 17%, especially for angles in the post-separated region.

2. Angle of Attack

The effect of α on the predicted Fr_x variation is investigated in this section. When the CFD simulations were done, the α was incrementally increased until flow separation was observed near the trailing edge. The observations

were made by checking the flow field plots around the simulated airfoil. From top to bottom, the subfigures of Figure 9 show the flow field plots around the NACA 0012 at α = 14°, 16° and 17°. These plots are for $Re = 1 \times 10^6$.

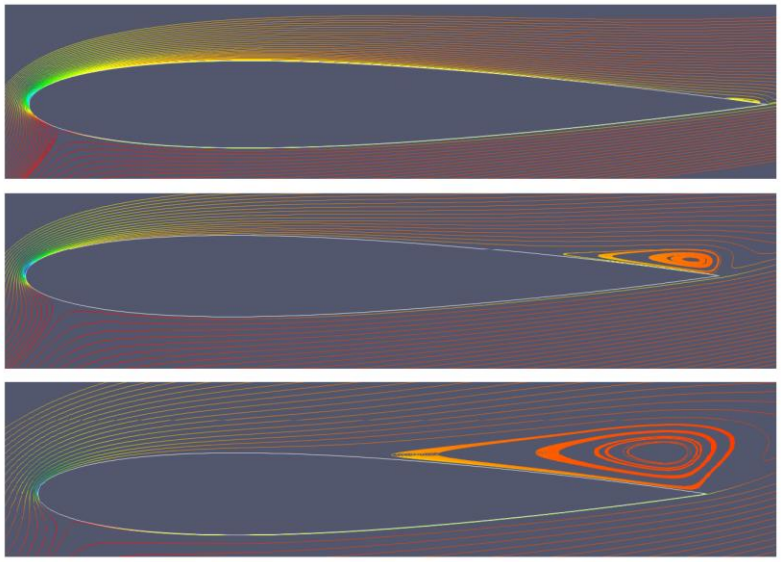

Figure 9 Flow Separation formation Near T.E. of NACA 0012 for α = 14°, 16° & 17°

As seen in Figure 9, a separation bubble is first observed near the trailing edge of the suction side at α = 14°. Although the bubble is very small at this angle, it is the first encounter with flow separation for $Re = 1 \times 10^6$. At the smaller simulated angles $0° \leq \alpha < 14°$, this phenomenon is not seen. For α = 16°, flow separation becomes more observable and a larger recirculation region within the bubble is seen. The separation point also moves away from the trailing edge and closer towards the leading edge of the airfoil. At α = 17°, the separation and corresponding recirculation continue to grow, becoming more significant. The separation point also continues to move closer towards the leading edge and can be seen around the mid-chord of the airfoil. For higher α up until the highest simulated α = 30°, the trend continued. Higher α produced larger recirculation regions and the separation point moved increasingly closer to leading edge, in accordance with what was determined by [21].

To translate the effect of an increasing α and the subsequent flow separation on the heat transfer estimation, the variation of the Fr_x versus S/c (for $Re = 1 \times 10^6$) on the suction side of the NACA 0012 is shown in Figure 10. Figure 10a shows the results at α = 0°, 5°, 10° and 16° while Figure 10b shows the results α = 16°, 20°, 25° and 30°. It is important to note that RANS predictions are not representative of physical flow for deep stall. In the context of this paper, the numerical predictions are used only to analyze the obtained Fr values.

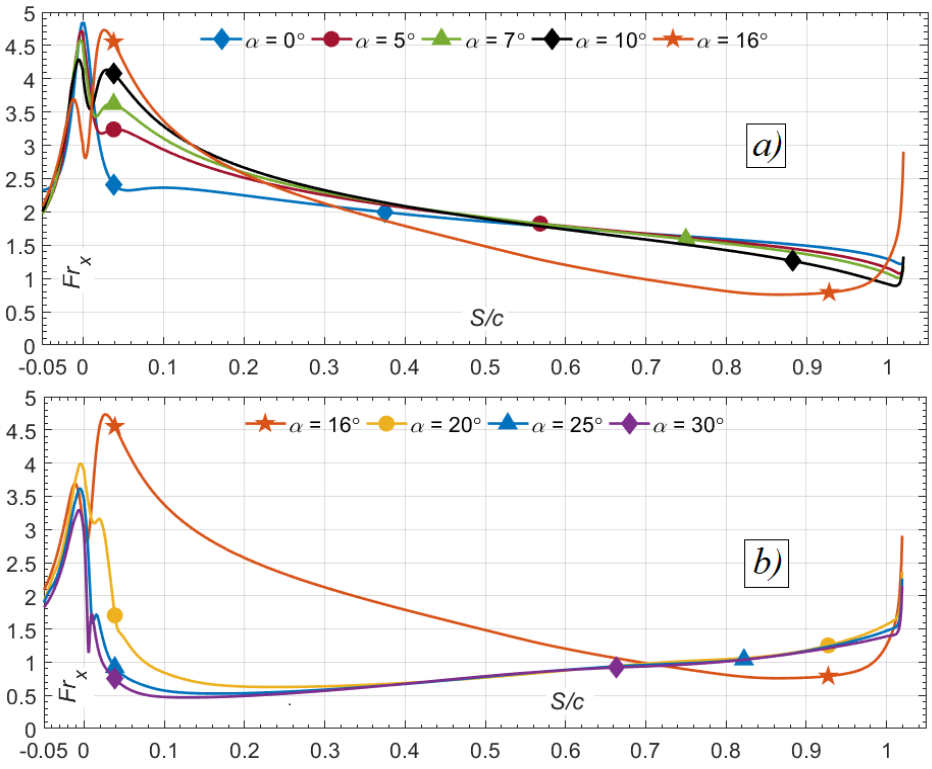

Figure 10 Fr_x Variation on NACA 0012 Wall for $Re = 1 \times 10^6$ at Various α

For $0° \leq \alpha < 16°$, the Fr_x increases near $S/c \approx 0.04$ when the α is increased. The Fr_x then decreases after $S/c \approx 0.04$ all the way to the trailing edge except for when $\alpha = 16°$. At this angle, the Fr_x is seen to change behavior and started increasing at $S/c \approx 0.9$. This behavior is parallel to the presence of flow separation in Figure 9. The recirculation region causes an enhanced mixing of the flow and causes the heat transfer rate to directly increase on the airfoil [21]. For $16° \leq \alpha < 30°$, flow separation continues to affect the heat transfer on the airfoil. Contrary to the smaller angles near $S/c \approx 0.04$, the Fr_x values drop as the α is increased. The separation point moved closer to the leading edge and the Fr_x decreases until $S/c \approx 0.1$. However, for $S/c \geq 0.1$ it is noted that Fr_x coincided for $\alpha = 20°$, 25° and 30° and kept increasing all the way to the T.E. of the airfoil. It is determined that at those angles, the flow separation becomes very large and the effect of flow recirculation has reached its limit.

3. Reynolds Number

The results of simulations indicated that the *Re* will increase the Fr_x regardless of S/c or α. This is illustrated in Figure 11, that shows the variation of the Fr_x versus the S/c of the simulated NACA 0012. The upper row shows the

test case at $\alpha = 0°$, the subfigure on the left is for the whole airfoil wall while the one on the right is a zoom, for a range of $-0.1 \leq S/c \leq \pm 0.1$. Similarly, the lower row shows the test case at $\alpha = 20°$, with a similar depiction of the S/c between the left and right subfigures.

For the case of $\alpha = 0°$, The Fr_x is highest at the stagnation point ($S/c = 0$) and a rapid drop of values is seen downstream till $S/c \approx \pm 0.04$. Afterwards, an increase in Fr_x is noted for $\pm 0.04 \leq S/c < \pm 0.08$ before a drop in values is continuously seen all the way to the trailing edge. Based on the results of CFD, an increase of Re caused the Fr_x to increase at all point except $S/c = 0$.

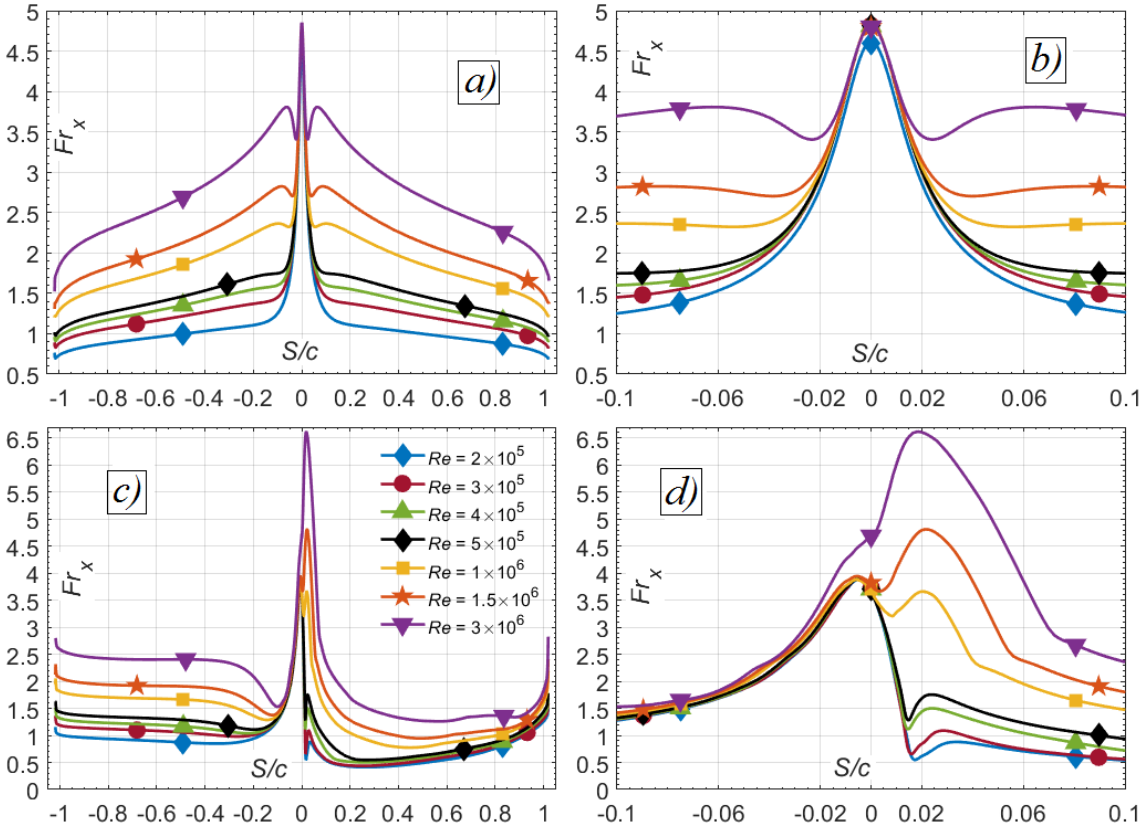

Figure 11 Fr_x Variation for a range of $2 \times 10^5 \leq Re \leq 3 \times 10^6$ at *a*) $\alpha = 0°$ (Whole Chord) and *b*) $\alpha = 0°$ (Leading Edge) as well as *c*) $\alpha = 20°$ (Whole Chord) and *d*) $\alpha = 20°$ (Leading Edge)

The same can be determined by checking the Fr_x variation at $\alpha = 20°$, with the difference in the stagnation point location. The positive α causes the stagnation point to move away from the leading edge on the bottom surface of the airfoil. For that case, the stretch of $-0.08 \leq S/c < -0.01$ shows unchanging values of Fr_x. Outside that range, the turbulent flow becomes dominant. For $S/c \geq -0.08$, the Fr_x increases before stabilizing at around a constant value

throughout the bottom surface towards the trailing edge. For $S/c \geq -0.01$, a significant increase in Fr_x is first encountered (due to increase in *Re*) before a drop in values continues till $S/c \approx 0.2$. For higher *S/c* (and depending on the *Re*), the Fr_x tends to increase all the way to the T.E. as a result of flow separation.

The two examined α correspond to the cases of a symmetric and attached flow ($\alpha = 0°$) from one side as well as an asymmetric and separated flow ($\alpha = 20°$) from the other. While the presented data at $\alpha = 0°$ and $\alpha = 20°$ show that the increasing *Re* caused the Fr_x to increase at the same *S/c*, this is true for all other simulated α. It is determined that for any other simulated α, an increase *Re* causes a direct increase in Fr_x, similar to what was seen for the turbulent correlations of the flat plate [14, 16].

IV. Discussion

A. Complete Results for the Fr_{Avg}

The complete results of the Fr_{Avg} for the simulations with constant T_S *TBC* and the SA_{TM} is presented in Figure 12. It shows the variation of the calculated Fr_{Avg} between $0° \leq \alpha \leq 30°$ and for $2 \times 10^5 \leq Re \leq 3 \times 10^6$. Results indicate that the Fr_{Avg} on the NACA 0012 under fully turbulent flow conditions follows a trend that is described by two behaviors: 1 - a direct increase in Fr_{Avg} values as the *Re* is increased, regardless of the α; and 2 – a continuous decrease in Fr_{Avg} values as the α is increased, regardless of the *Re*.

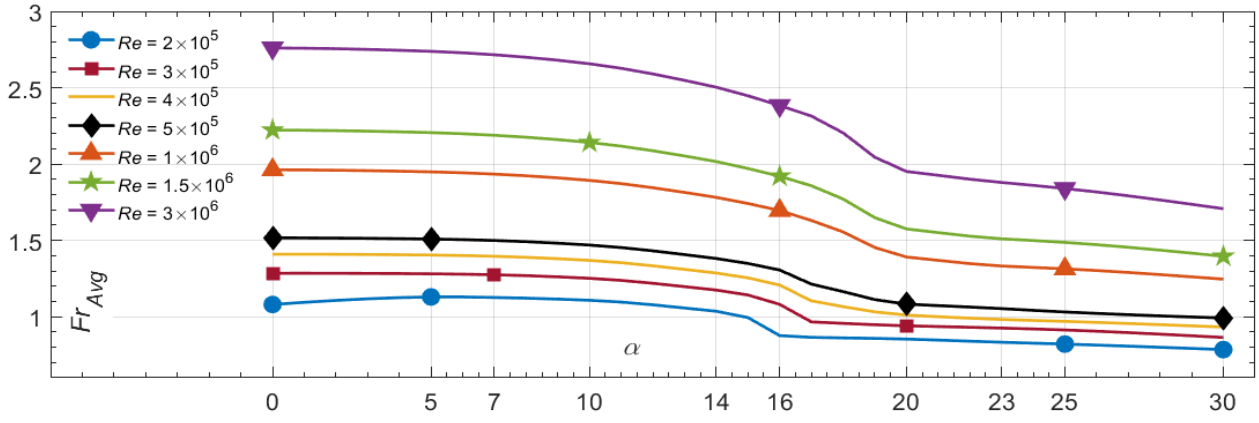

Figure 12 NACA 0012 Fr_{Avg} Variation of for $0° \leq \alpha \leq 30°$ & $1 \times 10^5 < Re < 3 \times 10^6$

Although it had been found that the Fr_x will increase near the leading edge on the upper side of the airfoil as the α increases, Figure 12 indicates that the average value of the *Fr* over the whole the airfoil will decrease. Moreover,

stall tends to make the Fr_{Avg} variation to become less steep and is strongly dependent on both *Re* and α. For *Re* = 2×10^5, this is seen to occur at α = 16° while for *Re* = 3×10^6, the effect is delayed up until α = 20°.

B. Novel Correlation for the Fr_{Avg}

The data from Figure 12 are correlated with *Re* and α based on the form of equation (11). The first step is to correlate the data at α = 0°, since the correlation would be then reduced to the form of $Fr_{Avg} = A\times \mathrm{Re}^{m}\times \mathrm{Pr}^{1/3}$. This way, the *A* and *m* can be determined first.

The curve fitting results are shown in Figure 13. It shows the Fr_{Avg} variation of the NACA 0012 versus the *Re*, as calculated from the CFD simulations as well as the correlation predictions. Curve fitting indicates that values of *A* = 0.021 and *m* = 0.335 would best fit the data. Therefore, at α = 0° and for a range of $2\times10^5 \le Re \le 3\times10^6$, equation (19) is obtained. The average error between the CFD values and correlation predictions is 0.53%. This way, the part of the correlation that concerns the variation of *Re* is developed and the effect of α is examined in the next section.

$$Fr_{Avg}\left(\alpha = 0°\right) = 0.021\times \mathrm{Re}^{0.335}\times \mathrm{Pr}^{1/3} \tag{19}$$

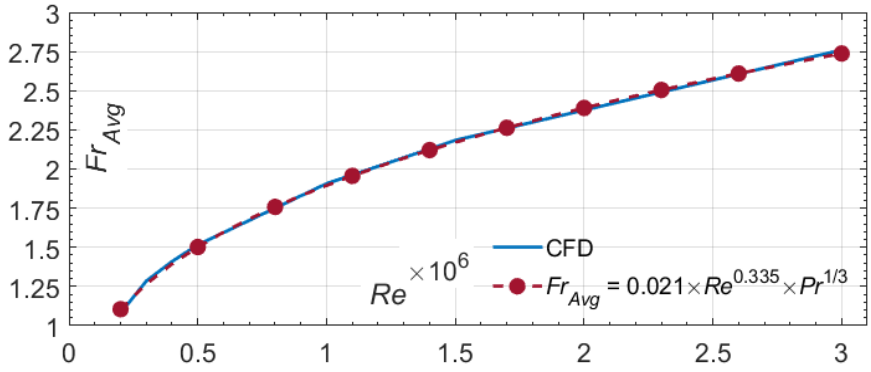

Figure 13 Curve Fitting of the Fr_{Avg} at α = 0° and $2\times10^5 \le Re \le 3\times10^6$

The next step of the correlation development is to quantify the variation of Fr_{Avg} with α. Specifically, the form of equation that describes the variation of the Fr_{Avg} (linear, quadratic or cubic) based on a varying α and a fixed *Re* is investigated. Recall that in the literature, a linear variation of α (equation (10) ref. [21]) was the only comparable form of correlation. Moreover, two sets of correlations were proposed, each for a specific range of *Re* (ref. [21]).

Figure 14 shows the Fr_{Avg} variation of the NACA 0012 versus the α as calculated from the CFD simulations. The values correspond to $Re = 1 \times 10^6$ and for a range of $0° \leq \alpha \leq 30°$. The figure also shows three other attempts of curve fittings based on the curve fitting of this work (equation (11)). A linear, quadratic, and cubic variation of α are compared in the figure to the results of the CFD simulations.

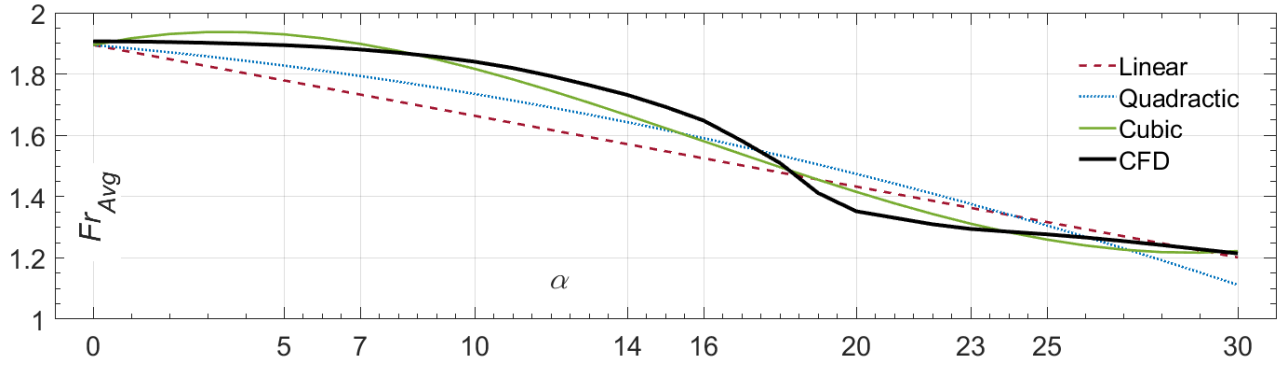

Figure 14 Curve Fitting Attempts for Different α Variations of the NACA 0012 Fr_{Avg} at $0° \leq \alpha \leq 30°$ and $Re = 1 \times 10^6$

Based on Figure 14, the linear and quadratic representations show the highest discrepancies from the Fr_{Avg} values, with an average error compared to the CFD values of 5.09% and 4.04%, respectively. Moreover, the maximum error for each was 12.71% and 17.38%. The cubic representation best fits the data with an average and maximum error value of 2.14% and 9.38%, respectively. It should be noted that fittings up to a quintic variation α have also been tried, but the cubic variation was favored for simplicity and since the impact on the average and maximum error values did not change by more than 0.2% for the fittings with higher orders.

The final form of the correlation to estimate the CFD-determined Fr_{Avg} is then described by equation (20). It represents a fully turbulent flow condition, with a constant T_S *TBC* and an average error of 2.14%. The correlation is valid for $0° \leq \alpha \leq 30°$ and $2 \times 10^5 \leq Re \leq 3 \times 10^6$. The α used in the correlation is in radians and $Pr = 0.71$.

$$Fr_{Avg} = 0.021\left(1 + 0.789\alpha - 7.408\alpha^2 + 8.795\alpha^3\right)\mathrm{Re}^{0.335}\,\mathrm{Pr}^{1/3} \tag{20}$$

From the other hand and if the constant Q_S *TBC* is examined, the Fr_{Avg} values would be slightly lower than those of the constant T_S, according to the results of section C.1. The Fr_{Avg} values are 2% to 4% lower than for a constant T_S. While only one *Re* is studied under the constant Q_S compared to 7 different simulated *Re* for the constant T_S, the range of simulated α for both TBCs is the same. The trend of variation of the Fr_{Avg} versus α at $Re = 1 \times 10^6$ is also

similar for both *TBC*s. Therefore, a 3% decrease of Fr_{Avg} values as an approximation between the results of constant Q_S and constant T_S could be applied to equation (20), to calculate the Fr_{Avg} on the NACA 0012 with a constant Q_S *TBC*.

V. Conclusion

This paper presents a new correlation for Fr_{Avg} on a NACA 0012, under fully turbulent flow conditions. The correlation was created based on a heat transfer database that is the result of fully turbulent CFD simulations using the SA_{TM}. It offers a quick approach to calculate heat transfer on the NACA 0012 and is valid for a range of $2 \times 10^5 \leq Re \leq 3 \times 10^6$ and $0° \leq \alpha \leq 30°$. One possible use is for a coupling with low or medium-fidelity aerodynamic tools to predict heat transfer on the blades of a small helicopter tail rotor.

A flat plate test case was simulated to verify the CFD simulations. Correlation attempts of the CFD-based C_f and Fr showed agreement with empirical correlations from the literature, and the predicted Fr agreed within 2% to similar implementations of the SA_{TM} from the literature. On the other hand, lift and drag predictions of airfoil simulations were validated with experimental data (1.64% to 5.59% discrepancy) as well as other numerical implementations (0.73% to 1.12% discrepancy). The predicted Fr values of CFD at the stagnation point agreed within 8% of experimental NACA 0012 data.

When the Fr_{Avg} of the NACA 0012 simulations was analyzed, it was found to directly increase with Re and decrease with α, even when flow separation occurred. On the other hand, the use of a constant Q_S *TBC* showed that the Fr_{Avg} values would drop between 2% to 4%, compared to the constant T_S. Moreover, the Fr_{Avg} was consistent between the SA_{TM} and SST_{TM}, although a discrepancy between 5% and 17% existed, especially for angles in the post-separated region. The main contribution of this work was the proposed Fr_{Avg} correlation, based on the CFD simulations with SA_{TM}. The correlation parameters were determined by curve fitting at $\alpha = 0°$, and a later fitting of the Fr_{Avg} with α showed that a cubic variation would capture the data with an average error of 2.14%. The correlation is considered comprehensive enough to estimate the heat transfer on a 2D NACA 0012 airfoil, without the need to redo any CFD work. Future work for this research project is about elaborating the present CFD database into one that accounts also for transition effects. This would help also to quantify the heat transfer even for a laminar-to-turbulent transitional flow.

VI. Funding Sources

This research was funded jointly by the Consortium for Research and Innovation in Aerospace in Québec (CRIAQ) as well as Consortium for Aerospace Research and Innovation in Canada (CARIC) (Grant Number ENV-702), Natural Sciences and Engineering Research Council of Canada (NSERC) (Grant Number CRD 478088-14), Bell Textron Canada Ltd. and Socomore.

VII. Acknowledgments

We acknowledge the support provided by Calcul Québec (www.calculquebec.ca) and Compute Canada (www.computecanada.ca).

VIII. References

[1] Wright, W., *User Manual for LEWICE Ver. 3.2 of Work.* NASA Glenn Research Center, Cleveland, Ohio, 2008. https://ntrs.nasa.gov/search.jsp?R=20080048307.

[2] Montreuil, E., A. Chazottes, D. Guffond, A. Murrone, F. Caminade, and S. Catris. *ECLIPPS: 1 Enhancement of Prediction Capability in Icing Accretion and related Performance Penalties Part I: Three-dimensional CFD Prediction of the Ice Accretion*. in *1st AIAA Atmospheric and Space Environments Conference, 22-25 June 2009*. San Antonio, Texas, United States: American Institute of Aeronautics and Astronautics. https://doi.org/10.2514/6.2009-3969

[3] Guffond, D. and L. Brunet, *Validation du Programme Bidimensionnel de Capitation // Oce National D'Etudes et de Recherches Aerospatiales of Work.*, ONERA RP, 1988.

[4] Beaugendre, H., F. Morency, and W.G. Habashi, *FENSAP-ICE's three-dimensional in-flight ice accretion module: ICE3D.* Journal of Aircraft, 2003. **40**(2): p. 239-247. https://doi.org/10.2514/2.3113

[5] Gouttebroze, S., F. Saeed, and I. Paraschivoiu. *CANICE - Capabilities and Current Status*. in *NATO/RTO Workshop, Assessment of Icing Code Prediction Capabilities, Dec. 6-7, 2000*. Capua, Italy: CIRA. https://www.researchgate.net/profile/Farooq_Saeed/publication/228932401_Ice_Accretion_Simulation_Code_CANICE/links/56b5066208ae3c1b79ab1fef/Ice-Accretion-Simulation-Code-CANICE.pdf

[6] Morency, F., F. Tezok, and I. Paraschivoiu, *Anti-icing system simulation using CANICE.* Journal of Aircraft, 1999. **36**(6): p. 999-1006.

https://doi.org/10.2514/2.2541

[7] Habashi, W.G., M. Aubé, G. Baruzzi, F. Morency, P. Tran, and J.C. Narramore. *FENSAP-ICE: a fully-3d in-flight icing simulation system for aircraft, rotorcraft and UAVS*. in *24th International Congress of The Aeronautical Sciences, 29 August - 3 September 2004*. Yokohama, Japan.

http://www.icas.org/ICAS_ARCHIVE/ICAS2004/PAPERS/608.PDF

[8] Beaugendre, H., F. Morency, and W.G. Habashi, *Development of a second generation in-flight icing simulation code.* Journal of Fluids Engineering, 2006. **128**(2): p. 378-387.

https://doi.org/10.1115/FEDSM2003-45816

[9] Habashi, W.G., *Recent advances in CFD for in-flight icing simulations.* Japan Society of Fluid Mechanics, 2009. **28**(2): p. 99-118.

https://pdfs.semanticscholar.org/c425/00a34b46464392df2aee6f7f4260086b53ec.pdf

[10] Aliaga, C.N., M.S. Aubé, G.S. Baruzzi, and W.G. Habashi, *FENSAP-ICE-Unsteady: unified in-flight icing simulation methodology for aircraft, rotorcraft, and jet engines.* Journal of Aircraft, 2011. **48**(1): p. 119-126.

https://doi.org/10.2514/1.C000327

[11] Pendenza, A., W.G. Habashi, and M. Fossati, *A 3D mesh deformation technique for irregular in-flight ice accretion.* International Journal for Numerical Methods in Fluids 2015. **79**(5): p. 215-242.

https://doi.org/10.1002/fld.4049

[12] Pourbagian, M. and W.G. Habashi. *Parametric analysis of energy requirements of in-flight ice protection systems*. in *20th Annual conference of the CFD society of Canada, May 9-11, 2012*. Canmore, Alberta, Canada: CFD Society of Canada.

http://www.sinmec.ufsc.br/~dihlmann/MALISKA/proceedings_cfd_society_of_canada_conference_may_2012/papers/Pourbagian_Habashi.pdf

[13] Incropera, F.P., A.S. Lavine, T.L. Bergman, and D.P. DeWitt, *Fundamentals of Heat and Mass Transfer*. 7th ed. 2007, New York: John Wiley & Sons.

[14] Kays, W.M. and M. Crawford, *Convective Heat and Mass Transfer*. 3rd ed. 1993, New York: McGraw-Hill.

https://doi.org/10.1007/0-387-21803-3_9

[15] Lienhard, J., *Heat transfer in flat-plate boundary layers: a correlation for laminar, transitional and turbulent flow.* Journal of Heat Transfer, 2020. **142**(6).

https://doi.org/10.1115/1.4046795

[16] Poinsatte, P., *Heat transfer measurements from a NACA 0012 airfoil in flight and in the NASA Lewis icing research tunnel*, in *Department of Chemical Engineering*. 1990, University of Toledo: Ohio, United States.

https://ntrs.nasa.gov/api/citations/19900009887/downloads/19900009887.pdf

[17] Newton, J., J. Vanfossen, P. Poinsatte, and K. Dewitt. *Measurement of local convective heat transfer coefficients from a smooth and roughened NACA-0012 airfoil: Flight test data*. in *26th Aerospace Sciences Meeting, 11-14 January 1988*. Reno, Nevada, United States: American Institute of Aeronautics and Astronautics.
https://ntrs.nasa.gov/search.jsp?R=19880004170

[18] Henry, R.C., D. Guffond, F. Garnier, and A. Bouveret, *Heat transfer coefficient measurement on iced airfoil in small icing wind tunnel.* Journal of Thermophysics and Heat Transfer, 2000. **14**(3): p. 348-354.
https://doi.org/10.2514/2.6551

[19] Dukhan, N., K.J. De Witt, K. Masiulaniec, and G.J. Van Fossen Jr, *Experimental Frossling numbers for ice-roughened NACA 0012 airfoils.* Journal of Aircraft, 2003. **40**(6): p. 1161-1167.
https://doi.org/10.2514/2.7205

[20] Wang, X., G. Naterer, and E. Bibeau, *Experimental correlation of forced convection heat transfer from a NACA airfoil.* Experimental Thermal and Fluid Science, 2007. **31**(8): p. 1073-1082.
https://doi.org/10.1016/j.expthermflusci.2006.11.008

[21] Wang, X., G. Naterer, and E. Bibeau, *Convective heat transfer from a NACA airfoil at varying angles of attack*. Journal of Thermophysics and Heat Transfer, 2008. **22**(3): p. 457-463.
https://doi.org/10.2514/1.34405

[22] Li, G., E.J. Gutmark, R.T. Ruggeri, and J. Mabe, *Heat Transfer and Pressure Measurements on a Thick Airfoil.* Journal of Aircraft, 2009. **46**(6): p. 2130-2138.
https://doi.org/10.2514/1.44093

[23] Palacios, F., M.R. Colonno, A.C. Aranake, A. Campos, S.R. Copeland, T.D. Economon, A.K. Lonkar, T.W. Lukaczyk, T.W. Taylor, and J.J.J.A.p. Alonso. *Stanford University Unstructured (SU2): An open-source integrated computational environment for multi-physics simulation and design*. in *51st AIAA Aerospace Sciences Meeting including the New Horizons Forum and Aerospace Exposition*. Grapevine (Dallas/Ft. Worth Region), Texas, USA.
https://doi.org/10.2514/6.2013-287

[24] The MathWorks Inc. *Solve nonlinear least-squares (nonlinear data-fitting) problems*. 2019; Available from: https://www.mathworks.com/help/optim/ug/lsqnonlin.html.

[25] Dennis C. Jespersen, T.H.P., Marissa L. Childs, *OVERFLOW Turbulence Modeling Resource Validation Results of Work.*, NASA Ames Research Center, Moffett Field, CA 94035-0001, 2016.

[26] Spalart, P. and S. Allmaras. *A One-Equation Turbulence Model for Aerodynamic Flows*. in *30th Aerospace Sciences Meeting and Exhibit*. Reno, NV, U.S.A.
https://doi.org/10.2514/6.1992-439

[27] Menter, F.R.J.N.S.r.T.R.N., *Improved two-equation k-omega turbulence models for aerodynamic flows of Work.*, NASA Ames Research Center Moffett Field, CA, United States, Moffett Field, CA, United States, 1992. https://ntrs.nasa.gov/citations/19930013620.

[28] *NASA Langley Turbulence Modeling Resources*. 2017 [cited 2018 14 January]; Available from: http://turbmodels.larc.nasa.gov.

[29] Celik, I.B., U. Ghia, P.J. Roache, and C.J. Freitas, *Procedure for estimation and reporting of uncertainty due to discretization in CFD applications.* Journal of Fluids Engineering, 2008. **130**(7). https://doi.org/10.1115/1.2960953

[30] Diskin, B., J. Thomas, C.L. Rumsey, and A. Schwöppe. *Grid convergence for turbulent flows*. in *53rd AIAA Aerospace Sciences Meeting, 5-9 January 2015*. Kissimmee, Florida, USA. https://fun3d.larc.nasa.gov/papers/aiaa-2015-1746.pdf

[31] Aupoix, B. and P. Spalart, *Extensions of the Spalart–Allmaras turbulence model to account for wall roughness.* International Journal of Heat and Fluid Flow, 2003. **24**(4): p. 454-462. https://doi.org/10.1016/S0142-727X(03)00043-2

[32] Abdollahzadeh, M., M. Esmaeilpour, R. Vizinho, A. Younesi, and J. Pàscoa, *Assessment of RANS turbulence models for numerical study of laminar-turbulent transition in convection heat transfer*. International Journal of Heat and Mass Transfer, 2017. **115**: p. 1288-1308. https://doi.org/10.1016/j.ijheatmasstransfer.2017.08.114

[33] Jespersen, D.C., T.H. Pulliam, and M.L. Childs, *Overflow turbulence modeling resource validation results of Work.*, NASA Ames Research Center, Moffett Field, CA, USA, 2016. https://ntrs.nasa.gov/citations/20190000252.

[34] Ladson, C.L., *Effects of independent variation of Mach and Reynolds numbers on the low-speed aerodynamic characteristics of the NACA 0012 airfoil section of Work.*, NASA Langley Research Center Hampton, VA, USA, 1988. https://ntrs.nasa.gov/citations/19880019495.